Choosing an Optimal β Factor for Relaxed Eddy Accumulation Applications Across Vegetated and non-Vegetated Surfaces

Teresa Vogl[1,2], Amy Hrdina[3], and Christoph K. Thomas[2]

[1]University of Leipzig, Institute for Meteorology, 04103 Leipzig, Germany
[2]University of Bayreuth, Micrometeorology Group, 95440 Bayreuth, Germany
[3]Department of Civil and Environmental Engineering, Massachusetts Institute of Technology, Cambridge, MA, USA

Correspondence: Teresa Vogl (teresa.vogl@uni-leipzig.de)

Abstract. Accurately measuring the turbulent transport of reactive and conservative greenhouse gases, heat, and organic compounds between the surface and the atmosphere is critical for understanding trace gas exchange and its response to changes in climate and anthropogenic activities. The Relaxed Eddy Accumulation (REA) method enables measuring the land surface exchange when fast-response sensors are not available, broadening the suite of trace gases that can be investigated. ~~This study~~

5 ~~evaluates a variety of different REA approaches with the goal of formulating universally applicable recommendations for an optimal choice of the β factor in combination with a suitable deadband.~~ The β factor scales the concentration differences to the flux, and its choice is central to successfully using REA. Deadbands are used to select only certain turbulent motions to compute the flux.

This study evaluates a variety of different REA approaches with the goal of formulating universally applicable recommendations

10 for an optimal choice of the β factor in combination with a suitable deadband. Observations were collected across three contrasting ecosystems offering stark differences in scalar transport and dynamics: A mid-latitude grassland ecosystem in Europe, a loose gravel surface of the Dry Valleys of Antarctica, and a spruce forest site in the European mid-range mountains. We tested a total of ~~three~~ four different REA models for the β factor: The first ~~method derives β_0~~ two methods, referred to as model 1 and model 2, derive β_p based on a proxy p for which high-frequency observations are available (sensible heat~~). The second method~~

15 T_s). In the first case, a linear deadband is applied, while in the second case, we are using a hyperbolic deadband. The third method, model 3, employs the approach ~~of~~ first published by Baker et al. (1992), which computes β_w solely based upon the vertical wind statistics. The ~~third method~~fourth method, model 4, uses a constant ~~β~~ $\beta_{p,const}$ derived from long-term averaging of the proxy-based ~~β_0~~ β_p factor. Each β model was optimized with respect to deadband type and size before intercomparison. ~~Concerning deadband form and size, we found an optimum in RMSE for linear deadbands with sizes of 0.5 and $0.9\sigma_w$. These~~

20 ~~deadband widths make this method approximately equal to the use of a constant β factor~~To our best knowledge, this is the first study inter-comparing these different approaches over a range of different sites.

With respect to overall REA performance, we found that the β_w and constant ~~β from long-term measurements~~ $\beta_{p,const}$ performed more robustly than the proxy-dependent ~~approach β_0~~approaches. The latter ~~model~~ models still performed well when scalar similarity between the proxy (here ~~sensible heat~~T_s) and the scalar of interest (here ~~latent heat~~water vapour) show strong

25 statistical correlation, i.e. during periods when the distribution and temporal behavior of sources and sinks were similar. ~~With~~

~~respect to sensitivity of~~ Concerning the sensitivity of the different β factors to atmospheric stability, we observed that ~~β_0~~ β_T slightly increased with increasing stability parameter z/L when no deadband is applied, but this trend vanished with increasing deadband size. β_w was independent of z/L. To explain ~~these surprising differences~~ why the β_w approach seems to be insensitive towards changes in atmospheric stability, we separated the contribution of w' kurtosis to the flux uncertainty~~, which can be expressed by the median ratio of the REA flux compared to that from classical eddy covariance $\frac{F_{REA}}{F_{EC}}$. Results showed a strong sensitivity to site conditions: While the kurtosis of w' seems to have no effect on the flux estimate at the grassland site, decreasing trends with increasing kurtosis can be observed for the loose gravel and forests sites and could explain the variability of $\frac{F_{REA}}{F_{EC}}$ within 10%.~~.

For REA applications without deeper site-specific knowledge of the turbulent transport and degree of scalar similarity, we recommend using either the ~~constant β~~ $\beta_{p,const}$ or β_w models when REA scalar fluxes are not expected to be limited by the detection limit of the instrument. For conditions close to the instrument detection limit, the ~~β_0~~ β_p models using a hyperbolic deadband are the ~~optimum~~ recommended choice.

Copyright statement. TEXT

1 Introduction

Trace gases play a significant role in the atmosphere because of their relationship to human-induced climate change, their wide variety of natural and anthropogenic sources, and their impact on human and ecosystem health. Understanding their source and transport behavior is needed to better quantify, predict, and mitigate anthropogenic effects on the environment. The exchange of trace gases between the Earth's surface and the atmosphere is often the result of a combination of several biophysical processes and mechanisms. Observing the net turbulent exchange, i.e. the flux density of such gases can help identifying their sources and sinks, which in turn can help identifying their forcings. Micrometeorological techniques can measure area-integrated fluxes at the ecosystem level and are therefore suitable for computing atmospheric budgets of trace gases and aerosol species.

The most direct method to measure flux density, hereafter referred to as 'flux', between the surface and the atmosphere is the eddy covariance (EC) technique, which requires fast ($\geq$ 10 Hz) response sensors to capture all scales of turbulent eddies contributing to the flux. However, such sensors are not available for all trace gases of interest, particularly for reactive species with brief atmospheric lifetimes. In ~~such cases, eddy accumulation~~ these cases, Disjunct Eddy Covariance (DEC, Rinne and Ammann, 2012), i.e. non-continuous sub-sampling of the concentration and wind data series, offers one alternative to overcome this problem. Eddy Accumulation (EA) methods ~~, originally proposed by Desjardins (1972, 1977), were developed to provide an alternative means to~~ provide another solution for estimating the net flux ~~. A~~ of chemically more stable atmospheric species existing at very low concentrations. This technique was originally proposed by Desjardins (1972, 1977): In EA, a system of fast switching valves collects air into two separate reservoirs, i.e. one for upward moving eddies (updrafts, w_+) and one for downward moving eddies (downdrafts, w_-). However, in true eddy accumulation, the number of collected

samples must be proportional to the magnitude of the vertical wind speed. For systems with switching valves that are not fast enough to accommodate the shortest time scale of turbulent eddies and/or cannot perform proportional sampling, a relaxation of the original true EA technique is necessary by introducing a proportionality factor. The resulting indirect REA technique, as proposed by Businger and Oncley (1990), thus samples the air with a constant flow rate, dependent on the direction of vertical wind. While the first true EA system is currently under construction (Siebicke, 2016; Siebicke and Emad, 2019), REA approaches are a common and convenient alternative to direct flux measurement of EC and EA when fast-response analyzers for the gas species of interest are unavailable.

For the REA technique, the concentration difference between the two sample reservoirs, ~~$\Delta \bar{c} = (\bar{c_+} - \bar{c_-})$~~ $\Delta \bar{s} = (\bar{s_+} - \bar{s_-})$, in which ~~$c_+$~~ s_+ indicates the updrafts and ~~c_-~~ s_- the downdrafts, is linearly related to the vertical net flux F of the species of interest. Note that the term "concentration" refers to densities (expressed in e.g. $mmol\ m^{-3}$) throughout this paper. Due to the sampling relaxation, a linear proportionality factor, usually denoted by the Greek letter β, is required to compute the flux:

$$F_{REA} = \beta \cdot \Delta \bar{s} \cdot \sigma_w \tag{1}$$

with σ_w being the standard deviation of the vertical wind component w. This approach resembles flux-gradient similarity methods evaluated at a single height, where $\beta \cdot \sigma_w$ can be interpreted as an efficiency measure, relating the concentration difference of the scalar of interest to its flux. For practical and scientific reasons, several REA applications exclude samples associated with weak vertical wind speeds that fall into a certain range of values ("band") leading to an unsampled ("dead") region, which effectively acts as a filter (Fig. 1). Deadbands are applied with the intention of (i) increasing the concentration difference between updraft and downdraft reservoirs (Bowling et al., 1998), (ii) to avoid rapid switching between reservoirs due to small eddies and thus reduce the wear of valves, and (iii) to reduce the random noise in gas concentrations of sampled air, which is mostly due to the small-scale short-lived eddies with a minor flux contribution.

Since the choice of the β coefficient and the size and form of the deadband are critical to deriving biophysically meaningful flux measurements from REA, they have received much attention in the literature~~.~~: Dependency of β on the atmospheric stability z/L, where ~~L~~ L is the Obukhov length (Obukhov, 1946), turbulence and scalar similarity has been discussed, and approaches including fixed deadbands, constant β vs. dynamically adjusting β and/or the deadband to atmospheric conditions have been proposed (Businger and Oncley, 1990; Beverland et al., 1996; Katul et al., 1996; Andreas et al., 1998; Milne et al., 1999; Ammann and Meixner, 2002; Fotiadi et al., 2005; Ruppert et al., 2006; Held et al., 2008; Grönholm et al., 2008). The large number of potential combinations for the critical REA parameters and varying site conditions may often seem overwhelming to either the first-time user focusing on investigating the dynamics of a certain trace gas species or even to the advanced user lacking a detailed understanding of the site-specific turbulent flow conditions. To provide some science-based guidance, our study aims at giving a comprehensive overview covering the most common parameterizations of the β factor and the deadband with the goal of providing a practical selection guide for choosing an optimal β and deadband model by evaluating them across contrasting ecosystem types. Our choice of contrasting ecosystems is expected to increase the robustness of the findings. We evaluate the β models by simulating an idealized REA sampling applied to high time-resolution data of wind components and ~~and~~ scalar concentrations from field campaigns carried out over contrasting vegetated

and non-vegetated surfaces: The McMurdo Dry Valleys of Antarctica, which represent an almost exclusively physically driven ecosystem predominately covered by loose gravel, a biologically active grassland in direct vicinity to agricultural areas in Lindenberg, Germany, and the Waldstein spruce forest site in Germany, where measurements were carried out on a 33-m high tower. 'Idealized' REA sampling here means that any effects of instrument performance are neglected to isolate the flux

5 uncertainty solely related to choosing the critical REA parameters, i.e. β factor, and deadband size and type. We acknowledge that other challenges for measuring trace gas fluxes particularly of reactive components exist, which may substantially add to the uncertainty in REA flux estimates, including low detection limits, high precision demands, and other technical challenges posed by short-lived chemical species. A discussion of these sources of uncertainty are outside the scope of our study. However, even if the latter dominate selecting an optimal β model for a specific type of surface can still minimize the overall flux

10 uncertainty.

2 Theory of REA and overview of β parametrizations

2.1 Proxy ~~β_0~~ β_p model

The most commonly employed REA variant is based upon scalar-scalar similarity: Observations of a scalar ~~s~~ p, which is measured with fast-response sensors thus enabling the computation of the direct EC flux $\overline{~~w's'~~ w'p'}$, is used as a proxy for the

15 scalar of interest ~~c~~ s. The β factor needed for the simulated REA flux of ~~s~~ p to equal its measured EC flux is calculated and used for the flux computation of scalar ~~c~~ s. From this point on, we will refer to ~~β_0~~ it as β_p to represent this proxy approach:

$$\beta_{\underset{\sim}{0}p} = \frac{\overline{w's'}}{\sigma_w \cdot \Delta\overline{s}} \frac{\overline{w'p'}}{\sigma_w \cdot \Delta\overline{p}} \tag{2}$$

where ~~$\Delta\overline{s}$~~ $\Delta\overline{p}$ is the proxy scalar concentration difference between updrafts ($\overline{~~s(w>0)~~ p(w>0)}$) and downdrafts ($\overline{~~s(w<0)~~ p(w<0)}$). Often, sonic temperature $T_{\underset{\sim}{~~s~~ s}}$ is chosen as proxy scalar (e.g. Ren et al., 2011; Osterwalder et al., 2016, 2017) due to its avail-

20 ability and negligible measurement uncertainty. ~~The β_0~~

The β_p method is based on the strong assumption that the proxy scalar and the scalar of interest behave similarly in their exchange mechanism, which requires the vertical and horizontal distribution of the sinks and sources of both scalars to be identical. A violation of this assumption will inevitably lead to large errors in the REA flux estimate (Katul et al., 1995; Katul and Hsieh, 1999; Ruppert et al., 2006; Riederer et al., 2014). The similarity between ~~the scalar of interest and the scalar chosen~~

25 ~~as a proxy~~ s and p can be evaluated by examining the correlation coefficients between the high-resolution time series of the two scalars, if available. The scalar-scalar correlation coefficients, $r_{\underset{\sim}{~~cs~~ sp}}$, as used in other publications (e.g. Gao, 1995; Katul and Hsieh, 1999; Ruppert et al., 2006; Riederer et al., 2014), are defined as follows:

$$r_{\underset{\sim}{cs\,sp}} = \frac{\overline{c's'}}{\sigma_c \cdot \sigma_s} \frac{\overline{s'p'}}{\sigma_s \cdot \sigma_p} \tag{3}$$

4

2.2 Vertical wind statistics β_w model

An alternative ~~method to determine the β factor solely takes into account~~ REA method was originally derived by Baker et al. (1992), and Baker (2000) provided a comprehensive derivation. The technique rests upon the standard deviation ~~and difference of the mean vertical wind~~ statistics and was originally derived by Baker et al. (1992). We will refer to this approach as the β_w model, in which the proportionality factor is computed using the following relationship: of the vertical wind, and assumes velocity-scalar correlation. In brief, the flux is defined as:

$$\beta_w \overline{w's'} = \frac{\sigma_w}{\Delta\overline{w}} \cdot m \cdot \sigma_w^2 \tag{4}$$

~~Combining the above equations (1) and (7) yields the expression~~

$$F_{REA} = \frac{\Delta\bar{c}}{\Delta\overline{w}} \cdot \sigma_w^2 = m \cdot \sigma_w^2$$

~~which does not contain the β factor, but instead uses the slope~~ where m is the regression-estimated slope of the w' vs. s' correlation ~~(Baker, 2000). Compared to the proxy-estimated flux,~~. m can be approximated, using conditional sampling techniques, as

$$m = \frac{\Delta\bar{s}}{\Delta\overline{w}} \tag{5}$$

$\Delta\overline{w}$ is the difference of the mean vertical wind while sampling into the up- and downdraft reservoirs, respectively. This makes

$$F_{REA} = \frac{\Delta\bar{s}}{\Delta\overline{w}} \cdot \sigma_w^2 \tag{6}$$

and thus

$$\beta_w = \frac{\sigma_w}{\Delta\overline{w}}. \tag{7}$$

Above equations show that the scalar flux ~~becomes~~ is directly proportional to the vertical wind speed's variance σ_w^2, and thus to the turbulence statistics. This approach combines elements of the flux-gradient and flux-variance similarity theories.

The requirements for this parameterization are (i) a linear relationship between s' and w' through the origin, as well as (ii) the Gaussian distribution of the vertical wind velocity fluctuations. If both are fulfilled, ~~$\beta = 0.63$~~ $\beta_w = 0.63$, however, usually, smaller values of the ~~β~~ β_w parameter are measured (Katul et al., 2018).

The statistical moments of the w' distribution can be used to investigate deviations from ~~ideally Gaussian. The fourth-order moment of the w' distribution~~ an ideally Gaussian distribution. The fourth moment, i.e. the kurtosis or tailedness, has been explored by Katul et al. (1996), who found an increase of β_w with an increasing kurtosis of the w' distribution. Apart from excursions from an ideal Gaussian w' distribution, the s'-w' correlation also affects β_w. It was found that large energy-containing eddies (i.e. eddies with large w') are associated with smaller s' than predicted by the linear ~~$\Delta\bar{c}$~~ $\Delta\bar{s}$ vs. $\Delta\overline{w}$ fit,

resulting in the β_w method overestimating the scalar fluxes (Katul et al., 1996; Baker, 2000). Recently, Katul et al. (2018) disentangled effects due to intermittency of the vertical velocity and asymmetry of large coherent structures in w′ during the transport of ~~c~~s′, and were able to explain that β is smaller than the theoretical value of 0.63 when taking into account the sweep and ejection phases of coherent structures, which are subject to forcings other than those of the stochastic isotropic homogeneous background turbulence.

2.3 Dynamic deadband with constant ~~$\beta_{0,const}$~~$\beta_{p,const}$

Grönholm et al. (2008) proposed that a constant value of β can be used in REA flux calculation in combination with a dynamic linear deadband scaled by σ_w. A more detailed description of the deadband application can be found in ~~the subsequent section~~Section 2.4. The value of ~~β~~$\beta_{p,const}$ is derived by taking the median of ~~β_0 (of T_s or CO_2)~~β_p, $\hat{\beta}_p$, over a period of several days:

$$\beta_{\underset{\sim}{0,const}\,p,const} = \hat{\beta}_p, \tag{8}$$

~~where ˆ represents the median. This method was used~~ This method has e.g. been used by Osterwalder et al. (2016) to measure mercury fluxes at a peatland site.

2.4 Deadband models

Deadbands are widely used in REA applications. The use of a deadband can provide improved resolution ~~in~~ of concentration differences by selectively sampling eddies with a larger contribution to the trace gas exchange. The turbulence characteristics can differ greatly across different ecosystems, therefore, an optimal deadband size must be chosen carefully. In the β_w approach, they can limit the impact of weak "distorting" eddies, which contribute little to the flux. Thus, deadbands help improve the linearity of the ~~c~~s′-w′ relationship leading to a well defined m (see Eq. 6).

When applying a linear deadband to w′ (left panel in Fig. 1), no sample is taken if the magnitude of w′ is below a certain threshold. This threshold can be held constant or adjusted dynamically in time. Dynamical adjustments are often done by scaling with the standard deviation of the vertical wind ~~$a\,\sigma_w$,~~ σ_w. The linear deadband appears as two horizontal lines in the quadrant plot in Fig. 1 (left panel), defined by the linear equation

$$a \cdot \sigma_w + 0 \tag{9}$$

where a is a constant.

This approach offers the advantage of the deadband being proportional to the integral strength of the turbulent diffusive process transporting the trace gas of interest. During field sampling, the size of the deadband is dynamically adjusted by applying a back-looking running time window of fixed length to compute ~~$a\sigma_w$~~$a\,\sigma_w$. Baker (2000) recommends a linear deadband with a width of $a = 0.9$ to obtain the best estimate of the slope m in the β_w approach.

Hyperbolic deadbands ~~aim~~ are specifically designed to exclude eddies with little flux contribution and maximize the concentration difference between the two sampling reservoirs. The exclusion of up- or downdrafts is in this case not only based on
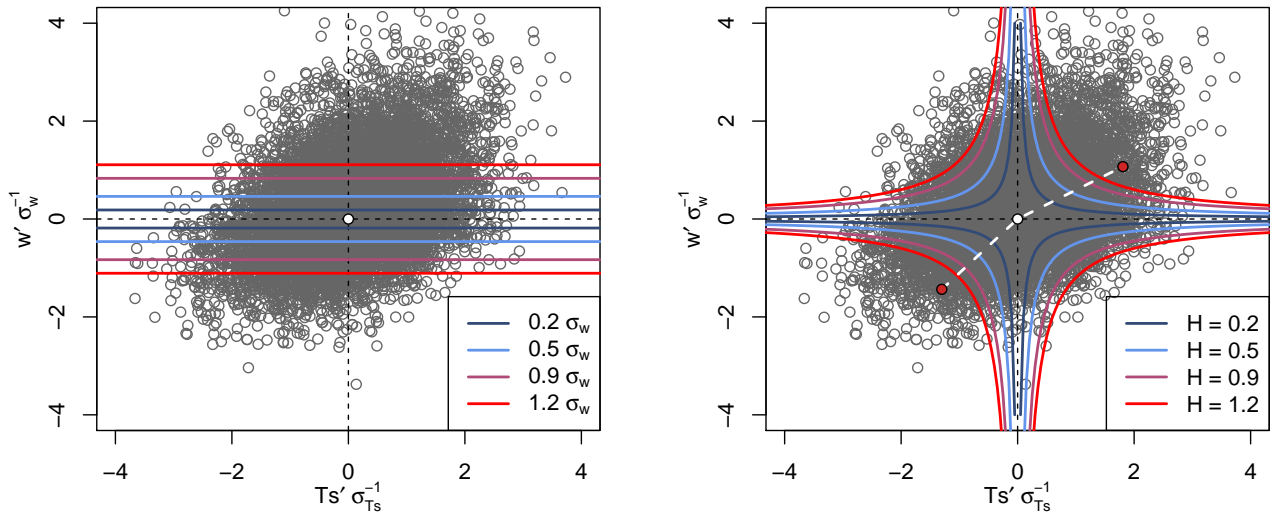
Figure 1. Schematic quadrant plots to visualize the application of linear (left) and hyperbolic (right) deadbands. Different ~~colors~~ colored lines show which data points are included for different deadband sizes. The white dot marks the origin in both panels. In the right-hand panel, solid ~~grey and~~ red dots mark the mean w'/σ_w and mean T_s'/σ_{Ts} for up- and downdrafts when ~~no deadband is applied (grey) and when~~ a hyperbolic deadband with $H = 1.2$ is applied (red). The white dashed lines in the right-hand panel connect the red dots with the coordinate system origin. The deviation from $180°$ of the angle spanned between these lines is ~~used as~~ a measure for the asymmetry of the sample distribution.

vertical wind velocity, but also on the fluctuations of a proxy scalar. Hyperbolic deadbands are defined by the dimensionless factor H ("hole size"), which is defined as ~~(Bowling et al., 1999):~~ in Bowling et al. (1999):

$$H = \frac{\overline{w's'}}{\sigma_w \cdot \sigma_s} \cdot \left| \left(\frac{w'}{\sigma_w}\right) \left(\frac{p'}{\sigma_p}\right) \right| \tag{10}$$

Plotting a such defined function in velocity-scalar space demonstrates that an area in the shape of two hyperbolas is excluded

5 (right panel in Fig. 1). The REA method using a hyperbolic deadband is often referred to as the HREA technique. Here, we only consider symmetrical deadbands, presuming symmetrically distributed flow and concentration statistics. Effects of non-Gaussian distributed w' and p' can be gleaned from investigating higher central statistical moments.
~~However, the~~ The use of large deadbands must be done with caution because they exclude a significant fraction of the data from being sampled~~, which could lead to increasing~~. As a result, the random sampling error~~caused by a decreasing sampling size,~~

10 ~~since it~~, which is related to $1/\sqrt{n}$, can be increased due to the decreased sample size n. In addition, the time period between opening and closing a sampling valve is reduced for large deadbands, which may introduce additional errors because of the

increased difficulty of sampling short-lived events precisely. An estimate for random error can be derived from the asymmetry of the sample distribution. Considering the quadrant plot of the data points sampled in one averaging period, the distribution can be represented by two points: $(\overline{s(w>0)}),(\overline{w(w>0)})$ and $(\overline{s(w<0)}),\ (\overline{w(w<0)})$. Considering the example in Fig. 1, these points are drawn in the right-hand panel for the largest deadband size (red dots)~~and for the null deadband (black dots)~~.

5 Ideally, these two points fall onto a unique linear relationship intersecting the coordinate system's origin (white dot). However, the use of large deadbands ~~leads to introducing~~ can introduce large asymmetry between up- and downdrafts~~and deviations from this expectation for the reasons mentioned above~~. The asymmetry is shown as a white dashed line in the right panel of Fig. 1, containing a bend. This bend, which can be expressed as an angle ~~deviating~~ different from $180°$, is ~~used as a~~ one measure for the asymmetry of the sample distribution~~in our study~~.

10 ## 2.5 Selected models and evaluation metrics

In this study, we compare β and deadband approaches used in literature and evaluate their performance for the prediction of the latent heat flux over different terrestrial surfaces. The following four REA methods have been chosen for the analysis:

– Model 1: ~~β_0~~ β_T (Eq. 2) using the sensible heat as proxy and a dynamically adjusted linear deadband scaled with σ_w (Eq. 9)

15 – Model 2: ~~β_0~~ β_T (Eq. 2) using the sensible heat as proxy and a dynamically adjusted hyperbolic deadband scaled with σ_w (Eq. 10)

– Model 3: β_w (Eq. 7) using a dynamically adjusted linear deadband scaled with σ_w (Eq. 9)

– Model 4: ~~$\beta_{0,const}$~~ ($\beta_{T,const}$ (Eq. 8; median over the complete field experiments) using sensible heat as a proxy and a dynamically adjusted linear deadband scaled with σ_w (Eq. 9)

20 For each of the models, ~~five~~ four different deadband widths ~~were~~ are examined both for linear ($0.2 \cdot \sigma_w$, $0.5 \cdot \sigma_w$, $0.9 \cdot \sigma_w$ and $1.2 \cdot \sigma_w$) and hyperbolic ($H = 0.2$, $H = 0.5$, $H = 0.9$ and $H = 1.2$) deadbands. One simulation was run as a control with a null deadband. To dynamically adjust deadband size, back-looking windows of 60 s and 300 s ~~durations~~ duration were tested. Comparison of these two window sizes yielded only negligible ~~difference~~ differences between the computed fluxes for the three datasets, hence we chose to present results from the 300 s window only.

25 ~~We proceded in the following fashion~~In the next steps, we proceed as follows: each of the above models is first optimized with respect to the deadband size. To do so, the accuracy of each β model is assessed by comparing the median ratio of the modeled flux, F_{REA}, and the corresponding direct EC-measured flux, F_{EC}, $\frac{F_{REA}}{F_{EC}}$: If this ratio is greater than 1, then the flux is overestimated by the model, and if it is < 1, the flux is underpredicted. In addition, the variability of this ratio is inferred using the root mean square error (RMSE), which provides a measure of the precision of each model. It is computed using the

30 difference between the modeled REA flux and the measured EC flux:

$$RMSE = \sqrt{\frac{\sum\limits_{i=1}^{n} (F_{REA,i} - F_{EC,i})^2}{n}} \tag{11}$$

Table 1. Description of the three data sets used in this study, numbers from quality-screened data, aggregated to 30 min temporal resolution

surface type	Grassland	Loose gravel	Spruce forest
site	Falkenberg site, Lindenberg, Germany	McMurdo Dry Valleys, Antarctica	Waldstein site, ridge in the Fichtelgebirge Mountains in Bavaria, Germany
measurement period	2015-09-22 to 2015-10-01	2012-12-26 to 2013-01-26	2016-06-18 to 2016-07-17
lat/lon	52.17°N 14.12°E	77.57°S 163.48°E	50.13°N 11.87°E
elevation above sea level (a.s.l.) [m]	73	35	775
estimated surface roughness length (z_0)[m] according to Panofsky (1984)	~~4.46~~ 0.18	~~0.14~~ 0.06	~~65.45~~ 4.87
dynamic stability range (zL^{-1})	-1.95 to 9.38	-9.61 to -0.01	-6.74 to 3.96
horizontal wind speed ~~U~~ u [ms^{-1}]	0.06 to 3.67	0.11 to 6.44	0.32 to 6.50
IQR of friction velocity u_* [ms^{-1}]	0.047 to 0.205	0.126 to 0.256	0.371 to 0.730

The deadband width, which is found to yield the most accurate ~~latent heat~~ water vapor flux (taking into account relative error and RMSE), is then further evaluated. Table 2 summarizes the different tested model setups along with the optimal deadband sizes.

3 Sites and data processing

3.1 Site descriptions

We selected three sites with strongly contrasting vegetation cover and surface roughness, vegetation architecture, and biogeochemical processes governing the vertical exchange of CO_2, water vapor and sensible heat to test the different β models (Table 1). Using sites with stark differences provides robust recommendations for REA users choosing an optimal β for their site.

The grassland data (Thomas et al., 2021) ~~was~~ were collected in Falkenberg, Germany at the German Meteorological Service (Meteorological Observatory Lindenberg), (see Table 1 for details). The central part of the field site is a flat meadow of dimen-

sions 150 x 250 m covered by short grass (vegetation height $< 20\ cm$). This area is surrounded by grassland and agricultural fields in the immediate vicinity, a small village is situated about 600 m to the ~~SE~~southeast, and a small, but heterogeneous forest area lies to the west and northwest at about 1 to 1.5 km distance. Within the flux footprint of the tower, the main vegetation cover consisted of grassland and recently harvested maize. The soil type distribution in the area around Lindenberg is dominated by sandy soils covered by a layer of loam, which is typically found at a depth of between 50 cm and 80 cm. Lindenberg represents moderate mid-latitude climate conditions at the transition between marine and continental influences. Monthly mean temperatures (1961-1990) vary between 1.2°C (January) and 17.9°C (July), and the mean annual precipitation sum is 563 mm (Beyrich et al., 2002; Neisser et al., 2002).

In contrast, the McMurdo Dry Valleys (Thomas and Levy, 2021) span 4800 km^2 of ice-free land in Antarctica and are covered by rocks and glacial till (Linhardt et al., 2019). The area ranges from sea level to 2000 m in elevation composed of ice-covered lakes, short-lived streams, and rocky ice cemented soils that are surrounded by glaciers. ~~During calm conditions, the region is dominated by a strong near-surface temperature inversion. Strong katabatic winds draining the polar plateau frequently disrupt this inversion.~~ The mean annual temperature in the Dry Valleys ranges between -17 and -20°C. The low precipitation relative to potential evaporation, low surface albedo, and dry katabatic winds descending from the Polar Plateau result in extremely arid conditions (Clow et al., 1998).

Finally, we use a data set acquired at a spruce forest site in the German Fichtelgebirge (Thomas and Babel, 2021) that spans ca. 1000 km^2 of north-eastern Bavaria, Germany. Its summits reach 1053 m a.s.l. (Schneeberg) and 1023 m a.s.l. (Ochsenkopf). The Waldstein hillsides comprise a mountainous ridge reaching up to 877 m a.s.l. (Gerstberger et al., 2004). The measurement site is located at about 800 m a.s.l.. The prevailing tree species at the Waldstein site is Norway spruce (*Picea abies, L.*) with a mean canopy height of 19 m. The flux measurements were conducted on top of a 31-m high scaffolding tower reaching above the highest tree tops, resulting in a total measurement height of 33 m above ground. Monthly mean temperatures (1961-1990) vary between -4.2°C (January) and 14.1°C (July), and the mean annual precipitation sum is 1156 mm (Foken, 2003).

Comparison of the ~~heat~~ kinematic heat, moisture and CO_2 fluxes ~~of~~ in the three ecosystems highlights the diverse exchange behavior trace gases can exhibit depending on the environments (Fig. 2)~~.~~: The differences in albedo and length of daylight are reflected in the variation in the sensible heat fluxes. The heat flux at the loose-gravel covered site in the Dry Valleys of Antarctica particularly stands out due to the perpetual sunlight experienced during the campaign period. A diel course is still observed, but is constantly directed away from the surface indicated by the positive values. The diel patterns ~~seen in both forest and grassland sites~~ visible at both the forest and the grassland site are similar, showing positive sensible heat flux during daytime and negative at nighttime. The difference in flux magnitude between forest and grassland can be attributed to the distinct differences in vegetative canopy properties. The tall dark canopy with low albedo surface is considerably different from the shorter and more reflective grassland canopy. The range in latent heat and CO_2 fluxes displays the impact of the vegetation. The loose-gravel site, which is the most extreme site void of vegetation, shows a net exchange of CO_2 equal or close to zero between the surface and the atmosphere, where both forest and grassland sites display an expected pattern of dominant CO_2 uptake during the daytime and respiration during the nighttime. The larger leaf area index in the forest of around 5 m^2m^{-2},
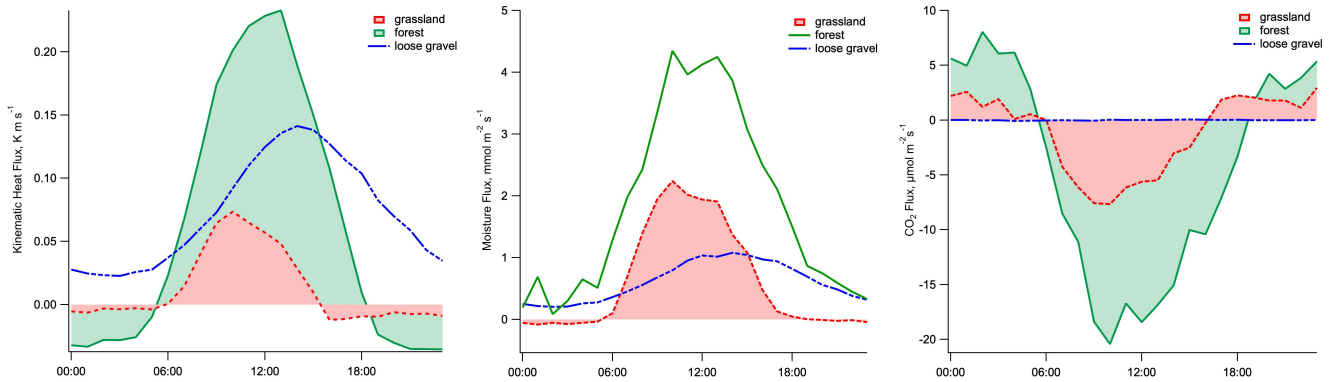
Figure 2. Ensemble-averaged diurnal fluxes of ~~sensible~~ kinematic heat flux (left panel), ~~latent heat~~ moisture flux (center panel) and CO_2 flux (right panel) at each of the three sites. The traces where the sign of the flux changes are filled to the zero line for clarity.

compared to $3\ m^2 m^{-2}$ for typical grassland areas, like in Lindenberg, causes a greater magnitude of latent heat flux because of the transpiration and concurrent greater exchange of CO_2.

3.2 Instrumentation and post-field data processing

The turbulence observations consisted of the three-dimensional wind vector and sonic temperature collected by a sonic anemome-
5 ter (Lindenberg: CSAT3, Campbell Scientific Ltd., Logan, UT, USA; Dry Valleys: 81000 VRE, R.M. Young Company, Traverse City, Michigan, USA; Waldstein forest: USA-1 FHN, Metek, Elmshorn, Germany) and water vapor and carbon dioxide molar densities measured by an open path analyzer (LI-7500, LI-COR Inc., Lincoln, NE, USA) both recorded by a data logger (CR3000, Campbell Scientific Ltd., Logan, UT, USA). The sampling rate was 20 Hz. Spikes and outliers in raw turbulence time series were discarded according to Vickers and Mahrt (1997) with an initial 5σ criterion. Resulting gaps in the high-frequency
10 time series were linearly interpolated. Covariances were maximized by shifting the scalar time series relative to that of the vertical velocity by a dynamically determined lag. This means that, for each sampling period, the scalar time series were shifted to achieve maximum cross-correlation with the vertical wind time series (Foken, 2008). For the Reynolds decomposition, a perturbation and averaging time scale of 300 s was chosen. Using this shorter than the common 30 min time scale is motivated by the intention to filter out the effects of longer-lived motions, as described in Vickers et al. (2009). Raw velocities were rotated
15 using the first two steps in the common 3D rotation method ensuring that the mean cross-wind and vertical wind components equal zero. A spectral correction was applied to EC fluxes following Moore (1986) to account for flux losses resulting from the sensor design and data collection. Quality assurance and quality control flags were applied to the computed REA and EC fluxes by testing for stationarity and developed turbulence following Foken et al. (2004). All data with flags > 1 were discarded from subsequent analysis. Since the flags do not capture all unphysical flux estimates, additional hard thresholding was applied. To
20 minimize the substantial random error in turbulent flux estimates over short averaging intervals, six subsequent 300 s intervals were block-averaged to yield one 30 min flux estimate for both the REA and EC method following Vickers et al. (2009).

Since simulating REA sampling requires selecting individual high frequency data from a continuous time series and computing density-corrected scalar higher-order moments, an *ad-hoc* density correction was applied to the water vapor and carbon dioxide molar densities (Detto and Katul, 2007) prior to flux computations. To this end, molar densities were multiplied by the ratio of the instantaneous to mean density of ~~moist air $\rho_q \overline{\rho_q}^{-1}$~~ dry air $\rho_a \overline{\rho_a}^{-1}$. This correction removes the density fluctuations due to changes in external conditions. EC fluxes were computed using the common *post-hoc* density correction (Webb et al., 1980). Even though open-path observations in cold environments such as the McMurdo Dry Valleys suffer from sensor heating artifacts not captured by either our *ad-hoc* or the common *post-hoc* WPL correction (Burba et al., 2008), we decided to not apply this additional correction in this study since we are interested in the relative flux error $(F_{REA} - F_{EC})F_{EC}^{-1}$ only. Instead, we applied a constant offset of 0.35 μmol m^{-2}s^{-1} to the CO_2 flux densities to force ~~it~~ them through zero for illustrative purposes. This choice has no effect on the study results.

For the REA flux estimation, hyperbolic and linear deadbands of varying sizes were tested. The linear deadband size was scaled by increasing fractions of σ_w computed over a back-looking running window of length 300 s (e.g., Ren et al., 2011; Arnts et al., 2013; Movarek et al., 2014). It must be noted that the deadbands are applied only to the w'-~~c'~~ s' statistics to compute ~~slope m~~ $\Delta \overline{s}$ and $\Delta \overline{w}$ (see Eq. (6)). In contrast, the entire population of vertical velocities observed in an averaging period were used to compute σ_w^2. Applying the deadbands for computing also the vertical velocity variance leads to significant flux overestimation since σ_w increases with increasing deadband size. In the final step, the same thresholds for physical plausibility which were applied to the computed EC fluxes were also used to remove unplausible REA flux estimates from the data sets. These thresholds were chosen individually for each scalar and each data set due to the wide range of meteorological and biochemical conditions covered in this study.

This study evaluates estimates of the latent heat flux $\overline{w'q'}$ obtained using different REA techniques. The approaches requiring a proxy scalar rely on the sensible heat flux $\overline{w'T'}$, which is common choice since it can be measured with a higher precision compared to e.g. CO_2 in certain low-flux conditions.

4 Results and Discussion

We structured this section ~~to first present~~ as follows: First, scalar correlation coefficients for the different ecosystems ~~in section~~ are presented in Section 4.1. In ~~section~~ Section 4.2, we describe the choice of an optimal deadband size for each REA model, based on both $\frac{F_{REA}}{F_{EC}}$ and the RMSE. The optimized REA models are then evaluated in ~~section~~ Section 4.3 with respect to the effects of the diurnal course and atmospheric stability. To test the applicability of our findings to other scalars, we are including an evaluation of simulated CO_2 REA fluxes for all four models, using T_s as proxy for models 1 and 2, in Appendix A. Here, the same deadband sizes are used, which were previously chosen as the optimum for the water vapor flux in Section 4.2 .

4.1 Scalar similarity across land surfaces

~~Since scalar~~ Scalar similarity is an important assumption for the β_0-β_T models (models 1 and 2)~~and as~~, and can be used as one evaluation metric for ~~our intercomparison, we first present the results on its temporal dynamics across land surfaces~~ the
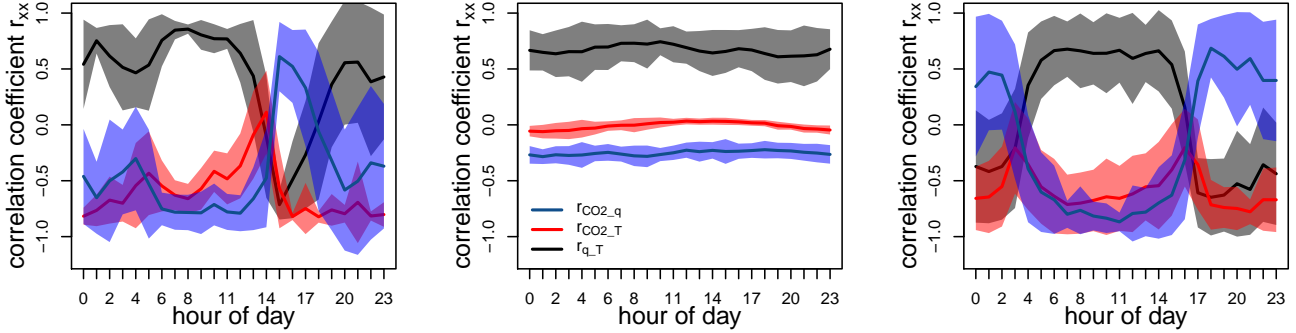
12

Figure 3. Diurnal course of scalar-scalar correlation coefficients $r_{\overline{x,y}_{sp}}$ at the meadow site (left panel), the loose gravel-covered Dry Valleys site (center panel) and the Waldstein forest site (right panel). $\pm$ one standard deviation σ is drawn as a semi-transparent area around the mean curves of $r_{\overline{x,y}_{sp}}$.

method. To assess whether a scalar can serve as a viable proxy p for the trace gas of interest s, the similarity in source and sink strength of two can be represented by their correlation coefficient $r_{\overline{x,y}}$ ~~(Ruppert et al., 2006).~~ $_{sp}$ (Eq. 3). We first analyze the temporal dynamics of scalar similarity across the different land surfaces: The diurnal courses of the correlation coefficients of $\overline{w'c'}$ and $\overline{w'T'}$, $\overline{w'c'}$ and $\overline{w'q'}$ and $\overline{w'T'}$ and $\overline{w'q'}$, ensemble-averaged over the complete field campaigns, are presented in Fig. 3. Pronounced temporal changes in scalar similarity within the diurnal cycle at the grassland and forest sites are in strong contrast to the constant values observed ~~$r_{\overline{x,y}}$~~ for all analyzed r_{sp} in the Dry Valleys~~(Fig. 3)~~. The patterns can be explained by the influence of radiative forcing, which governs both the physical heat exchanges and biological photosynthesis and evapotranpsiration, highlighting the constant daylight observed during the measurement period in the Dry Valleys. All three correlation coefficients change sign at the grassland site around 14:00 local time, associated with the expected change in dynamic stability resulting from the change in the direction of the sensible heat flux. A similar diurnal pattern is observed in the forest site, however, the change in sign of the correlation coefficient happens approximately two hours later in the day. In contrast, the correlation between $\overline{w'c'}$ and $\overline{w'q'}$ is positive throughout the nocturnal period in the forest site and negatively correlated in the grassland site, where regular dew formation occurs (which can be also observed in Fig. 2). The scalars tend to be poorly correlated at nighttime compared to daytime as a result of weak turbulence and associated diminished scalar transport efficiency for both sites.

4.2 Determining the optimal deadband size for each of the β methods

~~As expected,~~ Fig. 4 summarizes the effects of deadband size on the water vapor concentration difference between up- and downdraft reservoirs $\Delta\overline{q}$, and the fraction of samples used for flux computation, along with the asymmetry measure introduced in Section 2.4. As expected, $\Delta\overline{q}$ increases with increasing deadband size, for both linear and hyperbolic deadbands, at all
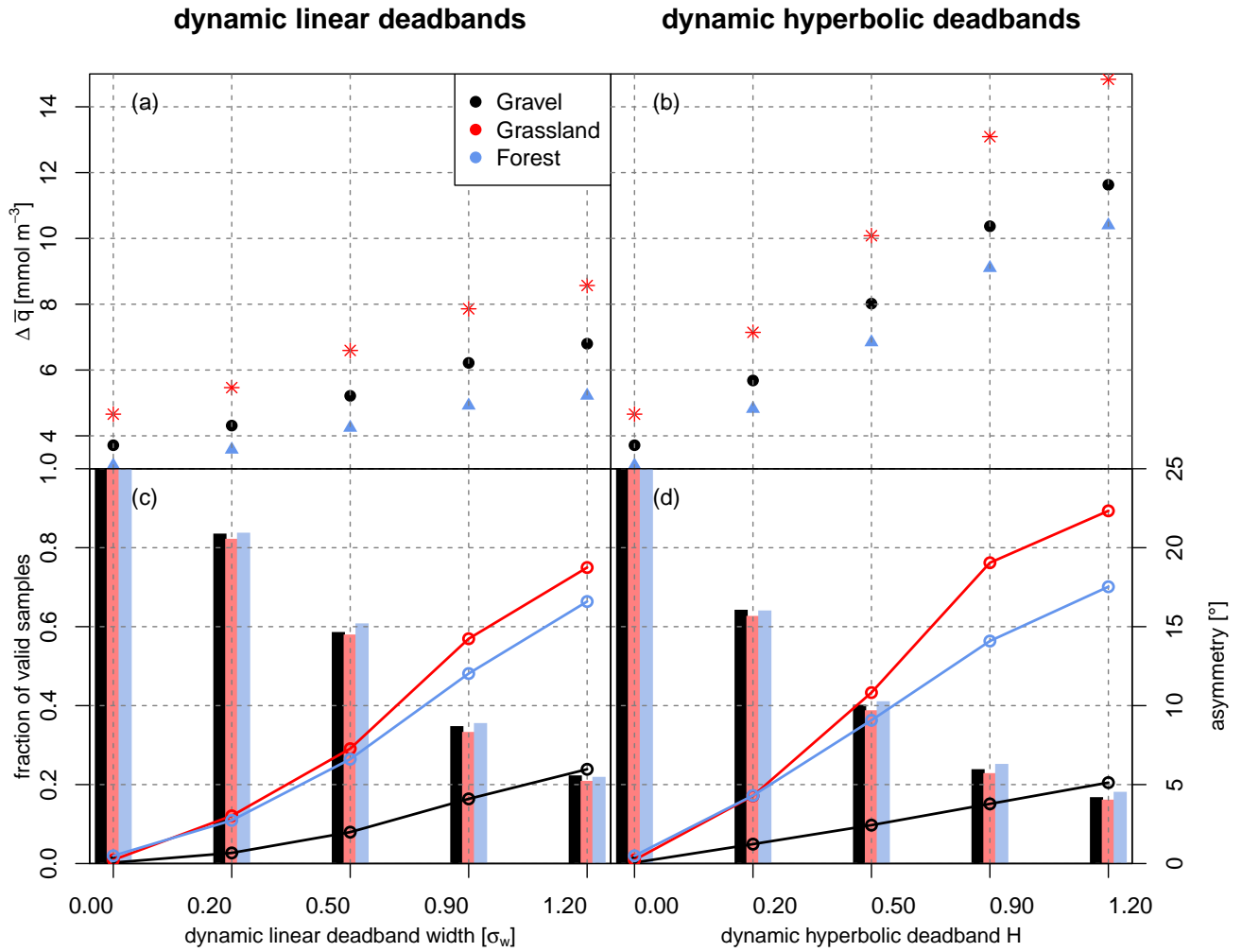
Figure 4. Effect of deadband size on the concentration difference and measures of the random error. The top two panels show the concentration difference between up- and downdraft reservoir as a function of deadband size (linear deadbands in left and hyperbolic deadbands in right panel); bottom panels: The bars show the fraction of samples used for flux computation and the overdrawn circles show the asymmetry between up- and downdraft vector in the quadrant plot. The asymmetry is calculated as the absolute deviation in the angle between a straight line and a bent line constructed using the center points of up- and downdrafts and the origin in the quadrant plots, see Fig. 1 and accompanying text for details.

three sites. This increase is more pronounced for hyperbolic deadbands compared to the linear deadbands (Fig. 4a and b). The hyperbolic deadbands have the desired effect of maximizing the concentration difference between the two sampling reservoirs. For $H = 1.2$, almost a factor of 3 increase in water vapor concentration difference between updraft and downdraft sampling reservoirs can be achieved. The HREA technique therefore has the potential to provide concentration differences detectable by instrumentation with high detection limits or when measuring chemical species with very low mixing ratios. However, as mentioned above, large deadbands can introduce a large random error because they exclude a large portion of the sample data points. The decrease in sample size with increasing deadband size is similar across all three sites (Fig. 4c and d) and should be considered when choosing an optimal deadband. For example, for a hyperbolic deadband with $H = 0.2$, approximately 40% of the sampling period is excluded, which results in an increased asymmetry (Fig. 4d). This effect is more pronounced for the forest and meadow surfaces than for the gravel site, possibly caused by a larger heterogeneity in scalar sink and source distribution.

In the next step, we evaluate each REA model individually and select an optimal deadband size with respect to selected uncertainty metrics of the β model~~.~~: We chose to include ~~both~~ measures of the precision and the accuracy of the methods by comparing $\frac{F_{REA}}{F_{EC}}$ and RMSE for the simulated deadbands. The ratio $\frac{F_{REA}}{F_{EC}}$ and RMSE obtained for different linear deadband widths using the ~~β_0~~ β_T model (model 1) are shown in Fig. 5. Results strongly vary ~~with ecosystem type~~ across the different ecosystem types: While the REA water vapor flux at the Antarctic gravel site is very similar to that obtained from the EC technique, ~~shown~~ as indicated by negligible RMSEs, the estimates obtained at the forest and meadow sites ~~have~~ feature a much larger RSME. This difference can be explained by the differences in the degree of scalar-scalar similarity between the latent and sensible heat fluxes of the purely physically driven site as opposed to the biologically active sites. The scalar fluxes are modulated by a varying degree of vegetation responses adding to the complexity of the scalar-scalar correlation $r_{q,T}$ and diurnal changes in sign (Fig 3). The use of no deadband (deadband width = 0) leads to an overall small underestimation of the EC fluxes (4 to 8%) across all sites. This underestimation is reduced with the use of a deadband at the gravel site; however, the systematic bias is not resolved by applying a deadband at the other two sites, but on the contrary increases this underestimation. Such a systematic bias could in theory be corrected for in post-processing, but the magnitude of the correction would have to be determined for each site defying our intention of providing general recommendations. This flux bias varies more between sites than with deadband width, therefore, this correction method should only be applied if the user knows the transport characteristics and scalar sink and source distribution well. Based on the flux bias and RMSE, a linear deadband with ~~0.2~~ 0.5 σ_w width is chosen as the optimized deadband size for further comparisons with the linear ~~β_0~~ β_T approach.

The results for the ~~β_0~~ β_T model using a hyperbolic deadband (model 2) are shown in Fig. 6. Both median F_{REA}/F_{EC} and RMSE are of the same order of magnitude compared to the linear deadband approach for ~~β_0~~ β_T (Fig. 5, model 1). However, the hyperbolic deadband offers an increase in concentration difference that is considerably larger ~~compared~~ in comparison, which led to its use in several studies (e.g. Held et al., 2008; Movarek et al., 2014). Interestingly, the observed underestimation of the latent heat flux is lessened for the forest and gravel sites when hyperbolic deadbands are applied, whereas it becomes larger for the meadow site. For the gravel site, the bias even changes sign for large hyperbolic deadbands. The RMSE shows no significant improvement when the small-scale eddies with small flux contributions are excluded irrespective of ecosystem.

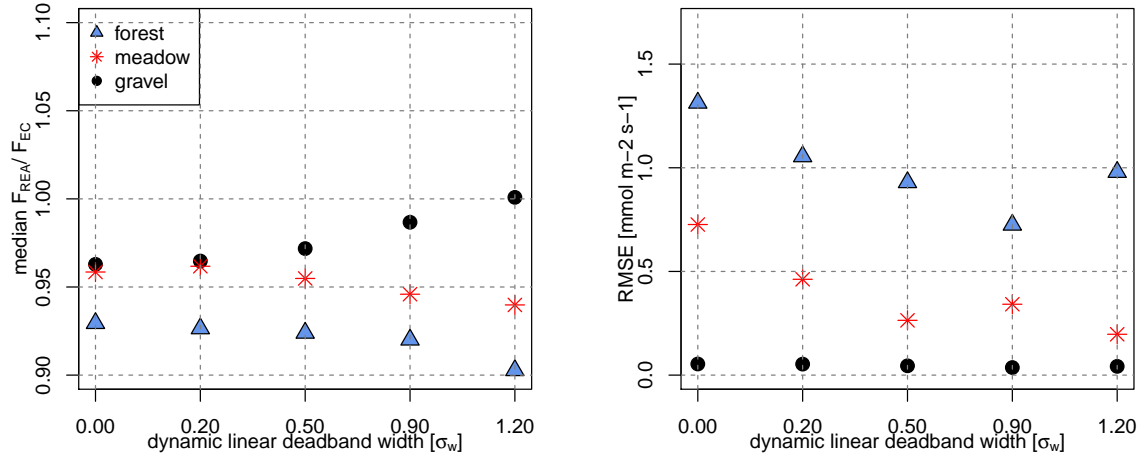## Dynamic linear deadband with β_T (model 1)

Figure 5. Errors as a function of dynamic linear deadband width. The x axis is the scaling factor a multiplied with the vertical wind standard deviation σ_w in Eq. 9 to define the deadband threshold. Left panel: Median F_{REA}/F_{EC} (latent heat flux simulated with sensible heat as a proxy) ratio for each of the simulated dynamic deadband widths; right panel: RMSE for each of the simulated dynamic deadband widths

Based on Fig. 6, a hyperbolic deadband of H = 0.5 is chosen for further analysis, as it offers an increase of $\Delta\overline{q}$ by 100% (Fig. 4). When applying a linear deadband to model 3 using β_w derived from the wind statistics alone, a positive flux bias (5-10%) ~~became~~ becomes evident when no deadband is applied (Fig. 7). This observation confirms the findings of Katul et al. (1996): ~~eddies~~ Eddies characterized by a large vertical perturbation (w′) are known to contain smaller perturbations in sensible heat

5 (T′$_s$) than predicted by the linear fit of $\Delta\overline{w}$ and $\Delta\overline{T_s}$, whose slope is dominated by the many small-scale eddies characterized by a greater T′$_s$. The use of deadbands puts more weight on large eddies, thus deadbands are convenient to improve the estimate of the w′ vs. T′$_s$ resulting in a smaller slope m for this model. The choice of deadband size has clear implications in how well the β_w model performs. ~~Note the different y-axis scales used in the right-panel graph of Fig. 7 compared to Figs. 5 and 6.~~ The RMSE for this method is ~~roughly two orders of magnitude smaller compared to~~ significantly smaller than the values

10 observed in the ~~β_0~~ two β_T models. Overall, the pattern in relative and absolute error is more consistent for the β_w model across the three ecosystems compared to the ~~β_0~~ β_T models. The optimal deadband width 0.9 σ_w, which was proposed by Baker (2000), provides low systematic bias, high precision, and the minimum in RMSE for all sites in Fig. 7. However, the use of this deadband size excludes more than 60% of the available data (see Fig. 4), so we chose a linear deadband width of 0.5 σ_w instead. This choice yields a similarly high accuracy and precision and therefore was our optimal choice for model

15 comparisons.

The performance of the constant ~~$\beta_{0,const}$~~ $\beta_{T,const}$ (model 4) is illustrated in Figure 8, in which the F_{REA}/F_{EC} and RMSE was calculated using a constant β and dynamic linear deadbands of different sizes. ~~Its RMSE issimilar~~ F_{REA}/F_{EC} is close
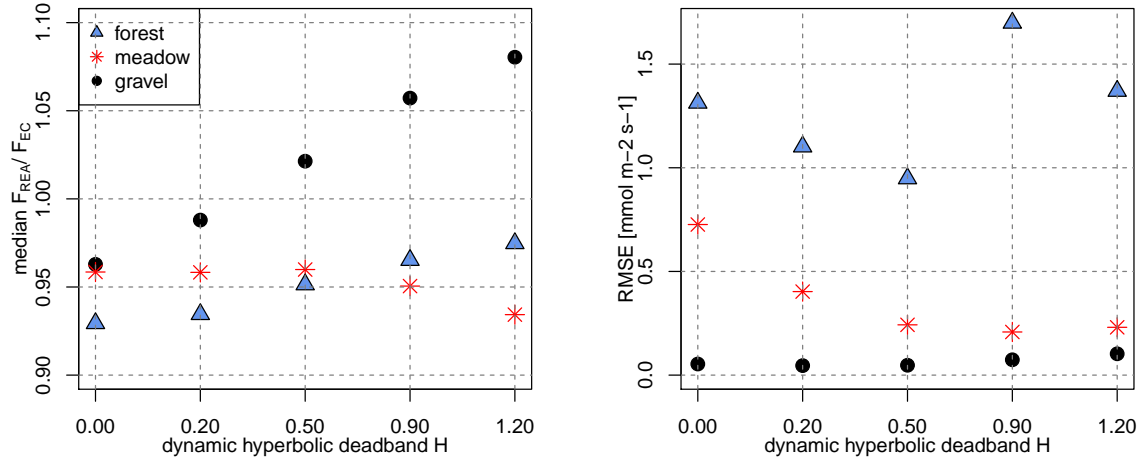
Figure 6. Errors as a function of dynamic hyperbolic deadband ~~width~~size. The x axis is the H parameter in Eq. 10, which defines the deadband size. Left panel: Median F_{REA}/F_{EC} (latent heat flux simulated with sensible heat as a proxy) ratio for each of the simulated dynamic deadband ~~widths~~sizes; right panel: RMSE for each of the simulated dynamic deadband ~~widths~~sizes

to 1 for all deadband sizes in this model. The RMSE is, similarly to that of the β_w (model 3~~) (~~, Fig. 7)~~with both in the order of magnitude and behavior with increasing deadband widths~~, constantly low for all ecosystems. Following Grönholm et al. (2008), we chose a deadband size of 0.5 σ_w for further comparison.

Table 2 summarizes the chosen optimum deadband widths for each of the four methods and gives the medians of the respective
5 β parameters for each of the three sites. The values for model 1 and model 4 are equivalent because the medians over the whole considered period are shown, which results in the definition of model 4.

4.3 Evaluation of optimized β models

After choosing an optimal deadband size for each REA model, we now proceed to analyzing the effects of the diurnal light variability and atmospheric stability on flux estimates.

10 #### 4.3.1 Effect of the diurnal course

Data were binned according to the hour of day and the RMSE was computed for each hour. Each panel in Figure 9 shows the result for the different ~~β models~~models 1–4 at the optimal deadband size. All four REA models successfully capture the flux at the loose gravel site, however, discrepancies between F_{REA} and F_{EC} become obvious for the meadow and forest sites. ~~Figure 9a and b show the RMSE of the two β_0 models using linear (model~~: Here, the RMSE for model 1 ~~) and hyperbolic (model~~and
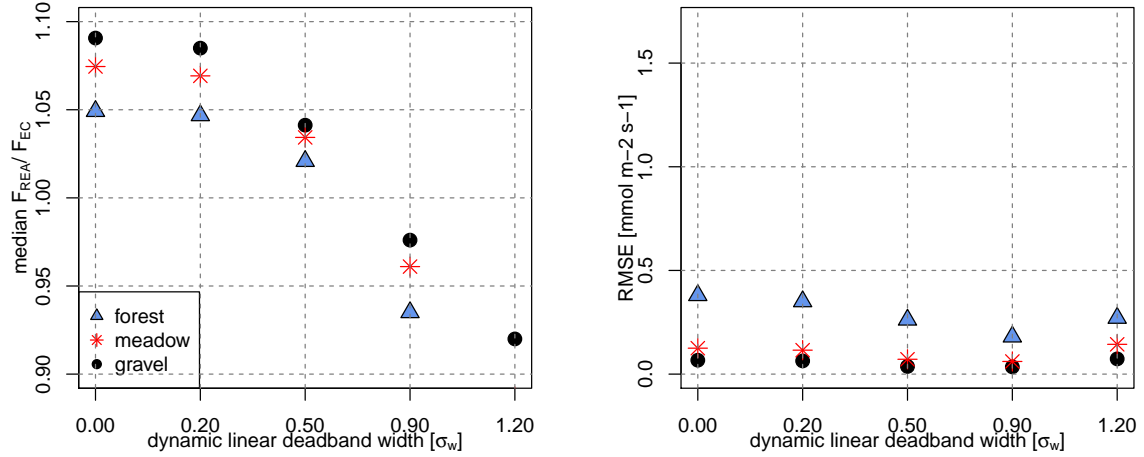
17

Figure 7. Errors as a function of dynamic linear deadband width. The x axis is the scaling factor a multiplied with the vertical wind standard deviation σ_w in Eq. 9 to define the deadband threshold. Left panel: Median F_{REA}/F_{EC} ratio (latent heat flux simulated using the REA approach described in Baker (2000)) for each of the simulated dynamic deadband widths; right panel: RMSE for each of the simulated dynamic deadband widths

Table 2. median β parameters for the chosen optimum deadband sizes for each of the four models and each of the three sites

model	β, deadband	meadow	gravel	forest
model 1	β_T, **linear deadband width** $\sigma_w = 0.5$	0.38	0.39	0.42
model 2	β_T, **hyperbolic deadband width** $H = 0.5$	0.25	0.26	0.27
model 3	β_w, **linear deadband width** $\sigma_w = 0.5$	0.43	0.43	0.44
model 4	$\beta_{T,const}$, **linear deadband width** $\sigma_w = 0.5$	0.38	0.39	0.42

model 2) deadbands.The error for these two methods (Fig. 9a and b) is significantly larger compared to the REA methods which are plotted in the bottom two panelsapplied by model 3 and 4 (Fig. 9c and d): The constant $\beta_{0,const}$ (model$\beta_{T,const}$ (model 4) and the β_w method (model 3), both utilizing a dynamic linear deadband, feature a negligible RMSE for the gravel and the meadow sites, and a small RMSE below unity for the forest site. The β_0 β_T models have a distinct peak in RMSE at the

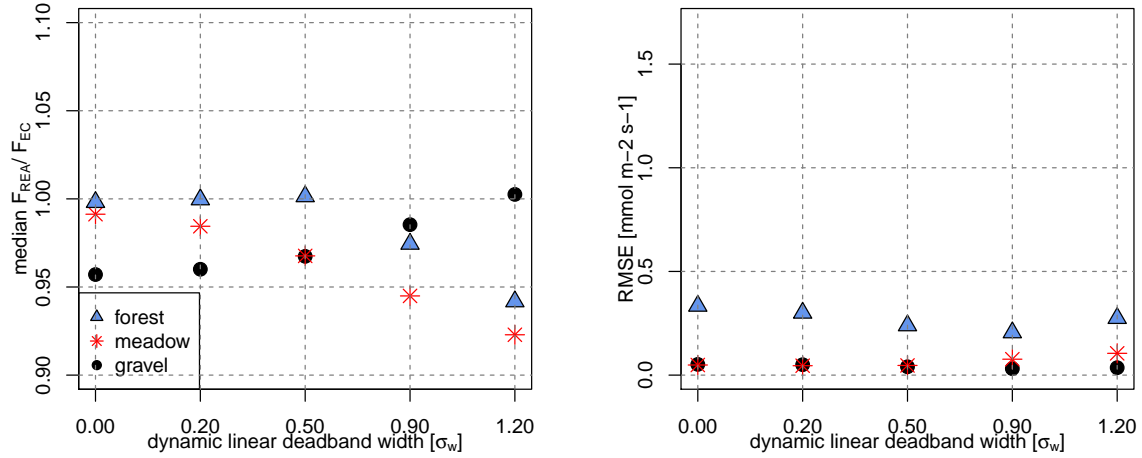## Dynamic linear deadband with constant β_T (model 4)

Figure 8. Median F_{REA}/F_{EC} ratio as a function of dynamic linear deadband width. The x axis is the scaling factor a multiplied with the vertical wind standard deviation σ_w in Eq. 9 to define the deadband threshold. Left panel: Median F_{REA}/F_{EC} ratio (latent heat flux simulated using constant β and dynamic linear vertical wind deadband) for each of the simulated dynamic deadband widths; right panel: RMSE for each of the simulated dynamic deadband widths

meadow site around 14:00 local time, which coincides with low scalar-scalar correlation of water vapor and heat (Fig. 3). At the forest site, the uncertainty in F_{REA} is large throughout the diurnal course for both β_0-β_T models due to the large variability in $r_{q,T}$. During times of strong variability, the difference F_{REA} - F_{EC} can be on the same order of magnitude as the absolute evapotranspiration. This occasional poor performance of the β_0-β_T model does not change significantly across the range of
5   tested linear and hyperbolic deadbands. Filtering out small-scale eddies therefore does not improve flux estimates. However, hyperbolic deadbands still increase the concentration difference $\Delta\bar{c}$ if the detection limit is of concern. Applying the REA proxy model for observing the diurnal variation of the exchange of a trace gas must be done carefully when choosing a proxy that exhibits a pronounced diurnal cycle. The key assumption in this approach is that the proxy and trace gas of interest have similar temporal or spatial dynamics, which introduces large uncertainties if the temporal dynamics of the scalar of interest
10   remain unknown or are not known a priori.

To test the applicability of the chosen optimized deadband sizes to other scalars, the CO_2 flux was simulated as well with the optimized models 1–4, using sensible heat as the proxy for models 1 and 2. The results for the hourly RMSEs are included in Appendix A in Fig. A1. Also in the case of CO_2, both proxy-based approaches yield higher RMSEs than the β_w and $\beta_{T,const}$ method.
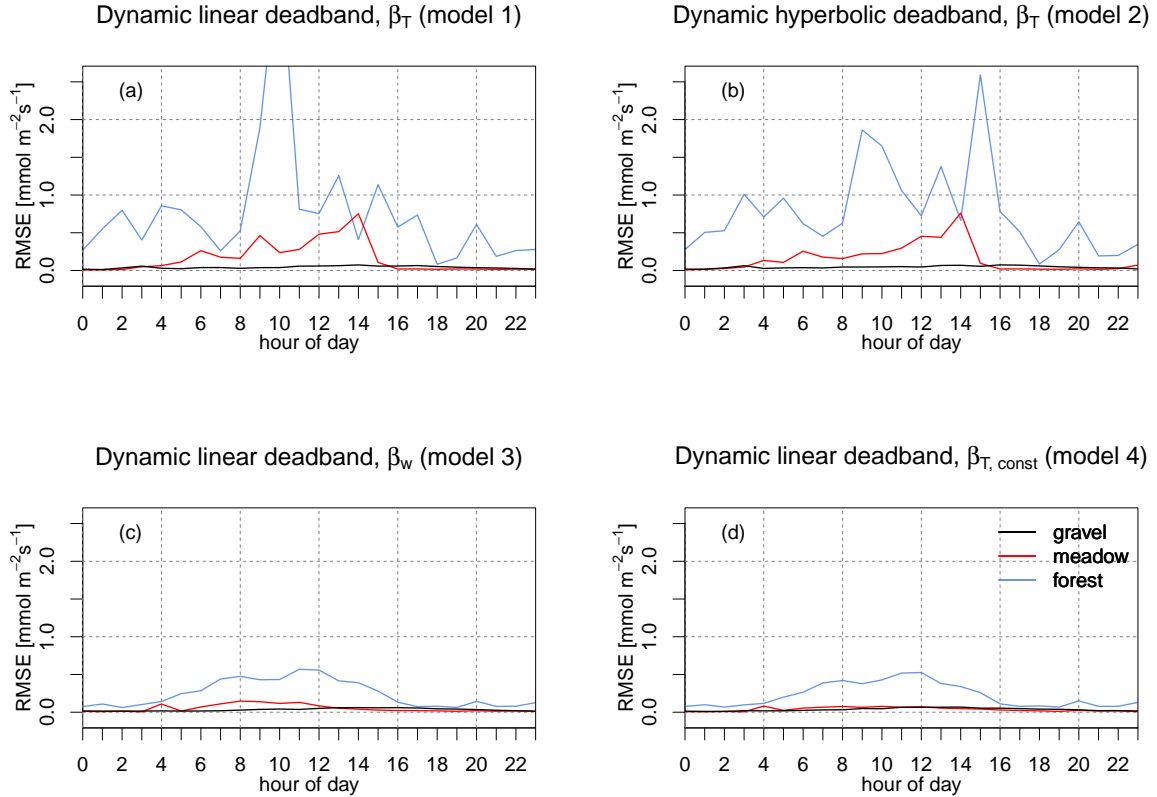
Figure 9. Flux RMSE as a function of the hour of day (local time) for each of the optimized β models. (a) shows the RMSE of the proxy-based model using a dynamically adjusted linear deadband (model 1), scaled with ~~$0.2\sigma_w$~~ $0.5\sigma_w$. In this panel, there is one extreme value with RMSE > 3, which is outside of the plot boundaries. (b) shows the proxy-based model using a dynamically adjusted hyperbolic deadband (model 2) with $H = 0.5$. ~~In this panel, there is one extreme value with RMSE > 3, which is not plotted.~~ (c) and (d) show the RMSE of the β_w REA model (model 3), and the constant ~~$\beta_{0,const}$~~ $\beta_{T,const}$ approach (model 4), respectively, both with a dynamically adjusted linear deadband of width $0.5\sigma_w$.
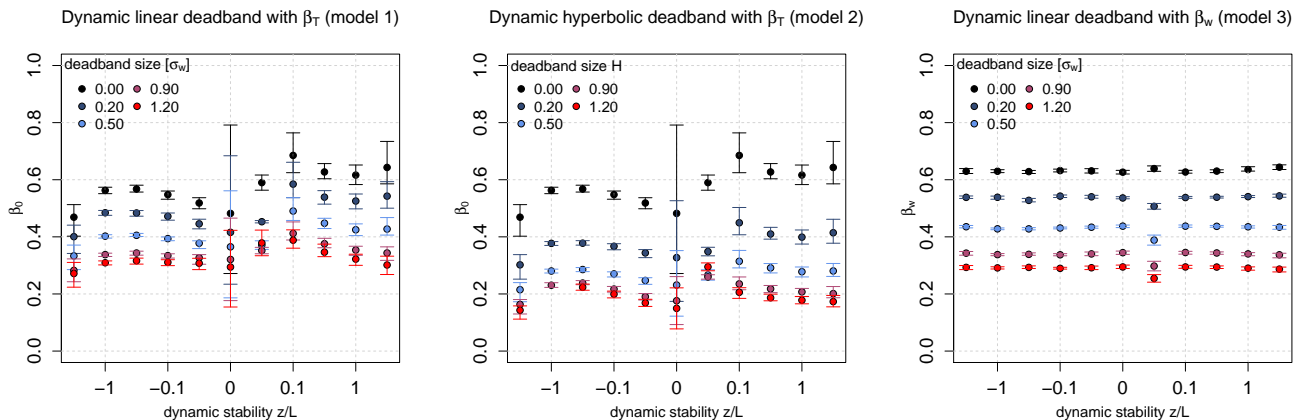
Figure 10. Dependence of the ~~β_0~~ β_T and β_w factors on the atmospheric stability z/L. Data were binned in logarithmic evenly spaced stability classes. The markers are drawn at the median β of each bin, the ~~arrows~~ bars mark the inter-quartile range (IQR). ~~The vertical dashed lines mark the boundaries of the neutral stability class, i.e. for the markers drawn at x=0. All other stability bins are spaced logarithmically in smaller intervals~~This figure combines valid data points from all three sites.

4.3.2 Effect of atmospheric stability

The observed relationship between the ~~β_0~~ β_T model bias and changes in scalar-scalar similarity suggests a dependence from shortwave radiative forcing leading to changes in atmospheric dynamic stability. A dependence of the ~~β_0~~ β_T factor on atmospheric stability has been shown in previous studies. Here, we extend this analysis to the effects of deadband type and size in addition to the β_w method. For comparison reasons, we evaluate the dependence of the β on dynamic stability (z/L) ~~using bins identical to those in~~ similar to Ammann and Meixner (2002) (their Fig. 3), who first documented a relationship between ~~β_0~~ β_T and atmospheric stability. Figure 10 shows the models for time-varying β ~~-~~binned into logarithmically spaced classes of dynamic stability. ~~The neutral stability class (markers drawn at z/L = 0) spans a larger stability range indicated by the two dashed vertical lines in each panel. For large deadbands, β decreases as the scalar concentration difference between up- and downdraft reservoir increases~~These classes were defined such that the range of dynamic stability spanned by each bin is equally sized in the logarithmic space. For the two proxy models (left and center panel in Fig. 10), ~~β_0~~ β_T follows the relationship found by Ammann and Meixner (2002) of a constant ~~β_0~~ β_T for unstable conditions, and an increase from neutral and stable conditions of $z/L \geq 0.06$. However, this increase is associated with large statistical uncertainty. We therefore recommend exercising caution when using stability-dependent parameterizations of ~~β_0~~ β_T for neutral and stable conditions. Ammann and Meixner (2002) analyzed data without a deadband (indentical to our deadband size $\sigma_w = 0$ and $H = 0$ in the left and center panels of Fig. 10). A similar trend is observed for the models with linear and hyperbolic deadbands. Variability of ~~β_0~~ β_T generally decreases with increasing deadband width. The β_w model (right panel in Fig. 10) shows significant differences compared to the proxy approaches: β_w does not change with dynamic stability and is less variable compared to that of ~~β_0~~β_T, as seen in the narrower
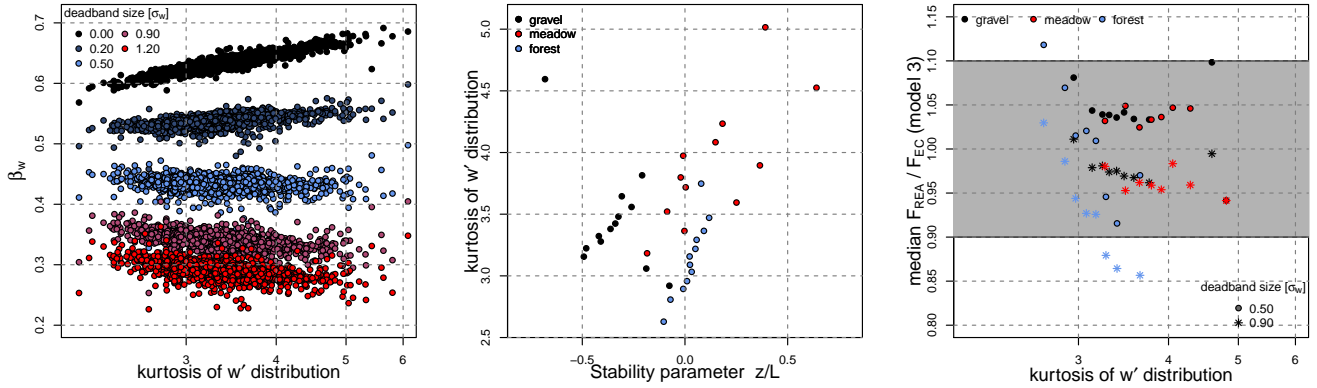
Figure 11. <u>This figure only presents results from REA model 3 (β_w).</u> Left panel: β_w as a function of w′ kurtosis for different deadband widths (not binned). <u>Valid data points from all three sites are combined in this panel.</u> Center panel: the stability parameter z/L as a function of the w′ kurtosis. Data were binned ~~by z/L prior to plotting and only~~ <u>into eight kurtosis bins with equivalent number of data points. Only</u> bin medians are displayed, <u>bars mark the IQR.</u> Right panel: Median F_{REA} by F_{EC} as a function of w′ kurtosis for the optimal deadband widths, $0.9\,\sigma_w$ and $0.5\,\sigma_w$, which were determined by Baker (2000) and in this study. Data were grouped into <u>the same</u> kurtosis bins <u>as in the center panel. The grey area marks the $\pm 10\%$ range, which is the error assumed in EC applications.</u>

spread of the ~~arrows~~ <u>bars</u> defining the inter-quartile range. This finding explains why the results in Figures 5, 8 and 9 for the β_w and constant β applying a dynamic linear deadband are so strikingly similar: β_w for the selected optimal deadband width of $0.5\sigma_w$ shows little variability, which makes this approach similar to applying a constant β factor.

~~As~~ <u>It was</u> pointed out in previous REA studies ~~,~~<u>that</u> β_w scales with the fourth central statistical moment of the vertical velocity

5   perturbations' distribution by altering the w′ vs. c′ relationship. We therefore investigated the impact of the w′ kurtosis on the β_w factor for different linear deadband sizes. Katul et al. (2018) found that two different factors, which both depend on z/L, contribute to β_w and whose impacts can cancel out if their magnitudes are similar. The first effect, leading to an decrease of β_w with increasing <u>(positive)</u> z/L, depends on the excess kurtosis, or flatness factor of the w′ distribution. The second effect, resulting in an increase of β_w with increasing z/L, is a result of the transport efficiency e_T (Wyngaard and Moeng, 1992), as

10   well as source strength and asymmetry in the w′ distribution. The superimposition of these two processes could be an explanation why there is no clear dependence of β_w ~~of~~ <u>on</u> dynamic stability visible in Figure 10. The relationship between the w′ distribution's kurtosis and the β_w factor is illustrated in Figure 11: consistent with Katul et al. (1996, 2018) the β_w factor without deadband increases as a function of w′ kurtosis (Fig. 11, left panel). The plot collapses data from all three ecosystems onto a single linear relationship. This finding suggests that the turbulence statistics are ubiquitous despite the significant differences

15   in climate and surface characteristics across the three ecosystems. The increasing linear trend becomes less pronounced when deadbands are applied.~~For the deadband size of $0.5\,\sigma_w$, no trend was found.~~

Kurtosis is in turn <u>expected to be</u> related to dynamic stability, ~~as can be seen in the center panel in Fig. 11: Changes~~ <u>when</u>

22

changes in turbulence statistics ~~with changing~~ and diabatic conditions lead to non-Gaussian distribution of w′. As a result, the kurtosis of the w′ distribution becomes different from 3, which is the ~~prediction~~ value for a Gaussian distribution. In the center panel in Fig. 11, w′ kurtosis is plotted against the stability parameter z/L. The right panel of Fig. 11 displays the resulting median $\frac{F_{REA}}{F_{EC}}$ as a function of w′ kurtosis. Only the model results for REA applying a linear deadband with widths of 0.5 and 0.9 σ_w are displayed here for improved visibility. While no clear trend ~~was~~ is observed at the grassland site, and only a slightly negative trend ~~was observed at~~ is visible for the gravel site, we ~~found~~ can detect a strong decrease of the median $\frac{F_{REA}}{F_{EC}}$ as a function of w′ kurtosis for the forest site. However, as is indicated by the shaded area in the rightmost panel of Fig. 11, most points lie within the boundaries of ± 10%. Only the bins with the highest and lowest kurtosis classes at the forest site are outside of this range. These error bounds are of the magnitude as the error assumed in EC applications. We suspect that the large excursions from Gaussian statistics for the forest site are caused by coherent structures forcing cross-canopy vertical exchange, which are a dominant flow mode in the forest flows documented for this site (Thomas and Foken, 2007a, b).

At first sight, it is puzzling why the β_w model without deadband (deadband size 0.00) in Fig. 11 shows a considerable variation with the kurtosis, which in turn is related to stability, but basically no dependence of the β_w factor on stability can be seen in Fig. 10. This effect is due to the binning: The values in the center panel of Fig. 10 are bin medians of the kurtosis, while in the left panel, the unbinned 30-minute data are shown. Comparing the ranges of the w-kurtosis in these panels, it becomes apparent that the range between 3 and 4 (Fig. 10 center) is much smaller compared to the range between 2 and 5 displayed in the left panel of Fig. 10. Within the approximate bounds of 3 and 4 (where most of the data are for all three sites), the β_w for zero deadband also has a much smaller systematic variability. Combining these insights with Fig. 10, it means that the bin median value of the w-kurtosis exaggerates the stability dependence, since the within-bin variability is very large, leading to its effect disappearing in the effective β_w (Fig. 10, right) and F_{REA}/F_{EC} (Fig 11, right) results. Our findings indicate that the variation of the β_w factor with the turbulence statistics seems to have no significant impact on the flux estimate.

5 Conclusions and practical recommendations

~~In this study , we~~ This study has compared the performance of four different conditional sampling models to compute the ~~scalar latent heat flux from conditional sampling simulations~~ water vapor flux. The tested REA models included the following methods: Two proxy-based approaches relying on the sensible heat T_s, using (i) linear and (ii) hyperbolic deadbands (models 1 and 2); (iii) a parameterization of the ~~β~~ β_w factor first introduced by Baker et al. (1992) (model 3), and (iv) an approach using a constant ~~β~~ β_T factor described in Grönholm et al. (2008) ~~. Table 2~~ (model 4). Models 3 and 4 both rely on linear deadbands. Deadbands were adjusted dynamically and simulated using a 300 s back-looking window to determine the standard deviation of the vertical wind σ_w, and, for the hyperbolic deadbands, the standard deviation of the proxy scalar T_s, σ_T. Table 3 summarizes the REA models investigated along with the main results of this study. The proxy-based (~~β_0~~ β_T) REA models (model 1 and 2) performed well during conditions when the proxy scalar (~~here sensible heat~~ T_s) and scalar of interest (~~here latent heat~~ water vapor) were strongly correlated, i.e. during periods when sources and sinks were similarly spatially distributed and temporally

Table 3. Summary of the REA models compared in this study, along with main findings

model #	model 1	model 2	model 3	model 4
~~summary description~~	β_0 ~~β_T~~ + linear deadband	~~β_0~~ β_T + hyperbolic deadband	β_w + linear deadband	constant β + linear deadband
optimal deadband size	~~0.2~~ $0.5 \cdot \sigma_w$	$H = 0.5$	$0.5 \cdot \sigma_w$	$0.5 \cdot \sigma_w$
site-specific effects	magnitude of underestimation differs between sites	positive or negative bias differs between sites	no strong site-dependent implications found; intermittent turbulence could have a weak effect on the accuracy of the method	no strong site effects
accuracy	within 8%	within 5%	within 5%	within 5%
precision	RMSE $\approx$ $1 mmol \ m^{-2}s^{-1}$ for biologically active sites	RMSE $\approx$ $1 mmol \ m^{-2}s^{-1}$ for biologically active sites	RMSE below $0.3 mmol \ m^{-2}s^{-1}$	RMSE below $0.3 mmol \, m^{-2}s^{-1}$
diel dependency	strong correlation with r_{xx}	strong correlation with r_{xx}	none	none
remarks		recommended when detection limit is an issue	robust method	robust method

synchronized. Median ratios $\frac{F_{REA}}{F_{EC}}$ over the campaign length were close to unity, indicating a generally high accuracy of ~~the methods. The diurnal course of the flux bias showed large deviations from the EC flux, particularly during transitions~~ these two methods. However, during times of low proxy-scalar correlation, the variability of this ratio, measured by the RMSE, was large. This happened particularly at those times of the day when the direction (sign) of the flux changed. ~~This increased~~
5 ~~variability vanishes when REA fluxes are ensemble-averaged over several diurnal cycles. However, users~~ Users are strongly cautioned when using the ~~β_0 proxy models. The~~ β_T proxy models; the diurnal dynamics of the proxy scalar and trace gas of interest is of central importance. This is also true for scalars subject to both biological and physical forcings driven by time- and space-variant source-sink distributions. Choosing the optimal proxy scalar is critical for the method's success. Hyperbolic deadbands, which also require the use of a proxy scalar, are well suited to maximize the concentration difference between up-
10 and downdraft reservoirs more effectively than linear deadbands. The effects of linear and hyperbolic deadbands on the flux estimates were found to be strongly site-dependent for the proxy-based approaches.

For the β_w ~~and constant $\beta_{0,const}$ models~~(model 3) and constant $\beta_{T,const}$ (model 4) approaches, an optimum deadband size was found ~~for~~ at 0.5 ~~and 0.9~~ σ_w. ~~In general, these two models performed more robustly than~~ At this deadband size, the variation of β_w became very small and was almost equal to applying a constant β factor. These two models yielded flux estimates as accurate as the proxy-dependent approaches. ~~The RMSE of these methods, which are utilizing dynamically adjusted σ_w-dependent linear deadbands, was orders of magnitude lower~~, and actually performed more robustly in terms of RMSE. The dependence on atmospheric stability conditions was evaluated for each method and deadband size. No universal behaviour of any stability-dependent (z/L) β model for either site was observed. We therefore cannot recommend its use.

Based on the findings obtained in this study, we attempt to formulate the following general recommendations: For applications without deeper site-specific knowledge, we recommend using either the β_w or $\beta_{T,const}$ approach (model 3 or model 4). These two models have been shown to perform robustly and be less sensitive to changes in proxy-scalar similarity than model 1 and 2. In case of a well-known site, including scalar-scalar similarity, we propose to use the proxy-dependent approach in connection with a hyperbolic deadband (model 2). Model 2 yielded very similar results to model 1 with respect to the precision and accuracy measures considered in this study. However, hyperbolic deadbands are better suited to maximize the concentration difference between up- and downdraft reservoirs, which is of advantage when investigating fluxes of compounds with very low atmospheric concentrations.

Data availability. data sets used are available at Zenodo: Thomas and Levy (2021), Thomas et al. (2021), Thomas and Babel (2021)

Appendix A: REA evaluations for the CO_2 flux
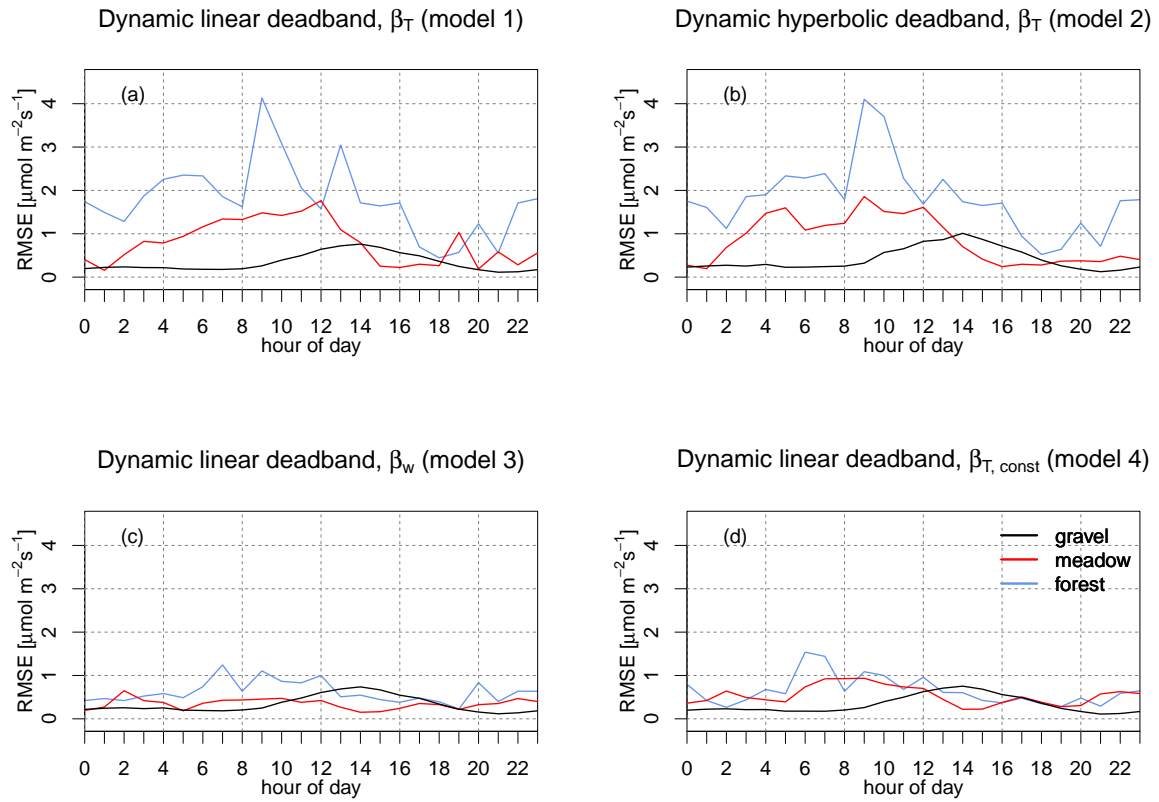
Fig. A1 shows the diurnal course of the RMSE

Figure A1. Same as Fig. 9 but for the CO$_2$ flux. The gravel site results (solid black lines) should be regarded with caution as the magnitude of the CO$_2$ flux at this site is close to zero (compare to Fig. 2)

5

References

Ammann, C. and Meixner, F. X.: Stability dependence of the relaxed eddy accumulation coefficient for various scalar quantities, J. Geophys. Res., 107, ACL7.1–ACL7.9, https://doi.org/10.1029/2001JD000649, 2002.

Andreas, E. L., Hill, R. J., Gosz, J. R., Moore, D. I., Otto, W. D., and Sarma, A. D.: Stability Dependence of the Eddy-Accumulation Coefficients for Momentum and Scalars, Boundary Layer Meteorol., 86, 409–420, https://doi.org/10.1023/A:1000625502550, 1998.

Arnts, R. R., Mowry, F. L., and Hampton, G. A.: A high-frequency response relaxed eddy accumulation flux measurement system for sampling short-lived biogenic volatile organic compounds, J. Geophys. Res. Atmos., 118, 4860–4873, https://doi.org/10.1002/jgrd.50215, 2013.

Baker, J. M.: Conditional sampling revisited, Agric. For. Meteorol., 104, 59–65, https://doi.org/10.1016/S0168-1923(00)00147-7, 2000.

Baker, J. M., Norman, J. M., and Bland, W. L.: Field-scale application of flux Measurement by conditional sampling, Agric. For. Meteorol., 62, 31–52, https://doi.org/10.1016/0168-1923(92)90004-N, 1992.

Beverland, I. J., Milne, R., Boissard, C., ÓNéill, D. H., Moncrieff, J. B., and Hewitt, C. N.: Measurement of carbon dioxide and hydrocarbon fluxes from a Sitka Spruce forest using micrometeorological techniques, J. Geophys. Res. Atmos., 101, 22 807–22 815, https://doi.org/10.1029/96JD01933, 1996.

Beyrich, F., Herzog, H.-J., and Neisser, J.: The LITFASS project of DWD and the LITFASS-98 experiment: The project strategy and the experimental setup, Theor. Appl. Climatol., 73, 3–18, https://doi.org/10.1007/s00704-002-0690-8, 2002.

Bivand, R.: classInt: Choose Univariate Class Intervals, https://CRAN.R-project.org/package=classInt, r package version 0.1-23, 2015.

Bowling, D. R., Turnipseed, A. A., C.Delany, A., Baldocchi, D. D., Greenberg, J. P., and Monson, R. K.: The use of relaxed eddy Accumulation to measure biosphere-atmosphere exchange of isoprene and other biological trace gases, Oecologia, 116, 306–315, https://doi.org/10.1007/s004420050592, 1998.

Bowling, D. R., Delany, A. C., Turnipseed, A. A., Baldocchi, D. D., and Monson, R. K.: Modification of the relaxed eddy accumulation technique to maximize measured scalar mixing ratio differences in updrafts and downdrafts, J. Geophys. Res. Atmos., 104, 9121–9133, https://doi.org/10.1029/1999JD900013, 1999.

Burba, G. G., McDermitt, D. K., Grelle, A., Anderson, D. J., and Xu, L.: Addressing the influence of instrument surface heat exchange on the measurements of CO_2 flux from open-path gas analyzers, Global Change Biol., 14, 1854–1876, https://doi.org/10.1111/j.1365-2486.2008.01606.x, 2008.

Businger, J. A. and Oncley, S. P.: Flux Measurement with conditional sampling, J. Atmos. Oceanic Technol., 7, 349–352, https://doi.org/10.1175/1520-0426(1990)007<0349:FMWCS>2.0.CO;2, 1990.

Clow, G. D., McKay, C. P., Simmons, G. M., and Wharton, R. A.: Climatological Observations and Predicted Sublimation Rates at Lake Hoare, Antarctica, J. Climate, 1, 715–727, https://doi.org/10.1175/1520-0442(1988)001<0715:COAPSR>2.0.CO;2, 1998.

Desjardins, R. L.: A study of carbon-dioxide and sensible heat flux using the eddy correlation technique, Ph.D. thesis, Cornell University, 1972.

Desjardins, R. L.: Description and Evaluation of sensible heat flux detector, Boundary Layer Meteorol., 11, 147–154, https://doi.org/10.1007/BF02166801, 1977.

Detto, M. and Katul, G. G.: Simplified expressions for adjusting higher-order turbulent statistics obtained from open path gas analyzers, Boundary-Layer Meteorol., 122, 205–216, https://doi.org/10.1007/s10546-006-9105-1, 2007.

Foken, T.: Lufthygienisch-Bioklimatische Kennzeichnung des oberen Egertales, Bayreuther Institut für Terrestrische Ökosystemforschung (BITÖK): Bayreuther Forum Ökologie, Selbstverlag, 100, 69+XLVIII, 2003.

Foken, T.: "Micrometeorology", Springer, 2008.

Foken, T., Göckede, M., Mauder, M., Mahrt, L., Amro, B., and Munger, W.: Post-Field Data Quality Control, in: Handbook of Micrometeo-
5   rology, edited by Lee, X., Massman, W., and Law, B., chap. 9, pp. 181–208, Kluwer Acadamic Publishers, 2004.

Fotiadi, A. K., Lohou, F., Druilhet, A., Serca, D., Brunet, Y., and Delmas, R.: Methodological Development of the Conditional Sampling Method. Part I: Sensitivity to Statistical And Technical Characteristics, Boundary Layer Meteorol., 114, 615–640, https://doi.org/10.1007/s10546-004-1080-9, 2005.

Gao, W.: The vertical change of coefficient b, used in the relaxed eddy accumulation method for flux measurement above and within a forest
10   canopy, Atmos. Environ., 29, 2339–2347, https://doi.org/10.1016/1352-2310(95)00147-Q, 1995.

Gerstberger, P., Foken, T., and Kalbitz, K.: The Lehstenbach and Steinkreuz Catchments in NE Bavaria, Germany, pp. 15–41, Springer Berlin Heidelberg, Berlin, Heidelberg, https://doi.org/10.1007/978-3-662-06073-5_2, http://dx.doi.org/10.1007/978-3-662-06073-5_2, 2004.

Grönholm, T., Haapanala, S., Launiainen, S., Rinne, J., Vesala, T., and Üllar Rannik: The dependence of the β coefficient of REA system with dynamic deadband on atmospheric conditions, Environ. Pollut., 152, 597–603, https://doi.org/10.1016/j.envpol.2007.06.071, 2008.

15   Held, A., Patton, E., Rizzo, L., Smith, J., Turnipseed, A., and Guenther, A.: Relaxed Eddy Accumulation Simulations of Aerosol Number Fluxes and Potential Proxy Scalars, Boundary Layer Meteorol., 129, 451–468, https://doi.org/10.1007/s10546-008-9327-5, 2008.

James, D. and Hornik, K.: chron: Chronological Objects which Can Handle Dates and Times, https://CRAN.R-project.org/package=chron, r package version 2.3-50. S original by David James, R port by Kurt Hornik., 2017.

Katul, G., Goltz, S. M., Hsieh, C.-I., Cheng, Y., Mowry, F., and Sigmon, J.: Estimation of surface heat and momentum fluxes using the flux-
20   variance method above uniform and non-uniform terrain, Boundary Layer Meteorol., 74, 237–260, https://doi.org/10.1007/BF00712120, 1995.

Katul, G., Finkelstein, P. L., Clarke, J. F., and Ellestad, T. G.: An Investigation of the conditional sampling methods used to estimate fluxes of active, reactive and passive scalars, J. Appl. Meteorol., 35, 1835–1845, https://doi.org/10.1175/1520-0450(1996)035<1835:AIOTCS>2.0.CO;2, 1996.

25   Katul, G., Peltola, O., Grönholm, T., Launiainen, S., Mammarella, I., and Vesala, T.: Ejective and Sweeping Motions Above a Peatland and Their Role in Relaxed-Eddy-Accumulation Measurements and Turbulent Transport Modelling, Boundary Layer Meteorol., 169, 163–184, https://doi.org/10.1007/s10546-018-0372-4, 2018.

Katul, G. G. and Hsieh, C.-I.: A Note on the Flux-Variance Similarity Relationships for Heat and Water Vapour in the Unstable Atmospheric Surface Layer, Boundary Layer Meteorol., 90, 327–338, https://doi.org/10.1023/A:1001747925158, 1999.

30   Linhardt, T., Levy, J. S., and Thomas, C. K.: Water tracks intensify surface energy and mass exchange in the Antarctic McMurdo Dry Valleys, The Cryosphere, 13, 2203–2219, https://doi.org/10.5194/tc-13-2203-2019, 2019.

Milne, R., Beverland, I. J., Hargreaves, K., and Moncrieff, J. B.: Variation of the beta coefficient in the relaxed eddy accumulation method, Boundary Layer Meteorol., 93, 211–225, https://doi.org/10.1023/A:1002061514948, 1999.

Moore, C. J.: Frequency response corrections for eddy correlation systems, Boundary Layer Meteorol., 37, 17–35,
35   https://doi.org/10.1007/BF00122754, 1986.

Movarek, A., Foken., T., and Trebs, I.: Application of a GC-ECD for measurements of biosphere-atmosphere exchange fluxes of peroxyacetyl nitrate using the Relaxed Eddy Accumulation and gradient method, Atmos. Meas. Tech., 7, 2097–2119, https://doi.org/10.5194/amt-7-2097-2014, 2014.

Neisser, J., Adam, W., Beyrich, F., Leiterer, U., and Steinhagen, H.: Atmospheric boundary layer monitoring at the Meteorological Observatory Lindenberg as a part of the Lindenberg Column: Facilities and selected results, Meteorol. Z., 11, 241–253, https://doi.org/10.1127/0941-2948/2002/0011-0241, 2002.

Obukhov, A.: 'Turbulentnost' v temperaturnoj–neodnorodnoj atmosfere (Turbulence in an Atmosphere with a Non-uniform Temperature)', Trudy Inst. Theor. Geofiz., https://doi.org/AN SSSR 1:95–115, 1946.

Osterwalder, S., Fritsche, J., Alewell, C., Schmutz, M., Nilsson, M. B., Jocher, G., Sommar, J., Rinne, J., and Bishop, K.: A dual-inlet, single detector relaxed eddy accumulation system for long-term measurement of mercury flux, Atmos. Meas. Tech., 9, 509–524, https://doi.org/10.5194/amt-9-509-2016, 2016.

Osterwalder, S., Bishop, K., Alewell, C., Fritsche, J., Laudon, H., Åkerblom, S., and Nilsson, M. B.: Mercury evasion from a boreal peatland shortens the timeline for recovery from legacy pollution, Sci. Rep., 7, https://doi.org/10.1038/s41598-017-16141-7, 2017.

Panofsky, H. A.: Vertical variation of roughness length at the Boulder Atmospheric Observatory, Boundary Layer Meteorol., 28, 305–308, https://doi.org/10.1007/BF00121309, 1984.

R Core Team: R: A Language and Environment for Statistical Computing, R Foundation for Statistical Computing, Vienna, Austria, https://www.R-project.org/, 2015.

Ren, X., Sanders, J. E., Rajendran, A., Weber, R. J., Goldstein, A. H., Pusede, S. E., Browne, E. C., Min, K.-E., and Cohen, R. C.: A relaxed eddy accumulation system for measuring vertical fluxes of nitrous acid, Atmos. Meas. Tech., 4, 2093–2103, https://doi.org/10.5194/amt-4-2093-2011, 2011.

Riederer, M., Hübner, J., Ruppert, J., Brand, W. A., and Foken, T.: Prerequisites for application of hyperbolic relaxed eddy accumulation on managed grasslands and alternative net ecosystem exchange flux partitioning, Atmos. Meas. Tech., 7, 4237–4250, https://doi.org/10.5194/amt-7-4237-2014, 2014.

Rinne, J. and Ammann, C.: Disjunct Eddy Covariance Method, pp. 291–307, Springer Netherlands, Dordrecht, https://doi.org/10.1007/978-94-007-2351-1_10, 2012.

Ruppert, J., Thomas, C., and Foken, T.: Scalar Similarity for Relaxed Eddy Accumulation Methods, Boundary Layer Meteorol., 120, 39–63, https://doi.org/10.1007/s10546-005-9043-3, 2006.

Ryan, J. A. and Ulrich, J. M.: xts: eXtensible Time Series, https://CRAN.R-project.org/package=xts, r package version 0.9-7, 2014.

Siebicke, L.: A True Eddy Accumulation - Eddy Covariance hybrid for measurements of turbulent trace gas fluxes, in: EGU General Assembly Conference Abstracts, vol. 18 of *EGU General Assembly Conference Abstracts*, p. 16124, 2016.

Siebicke, L. and Emad, A.: True eddy accumulation trace gas flux measurements: proof of concept, Atmos. Meas. Tech., 12, 4393–4420, https://doi.org/10.5194/amt-12-4393-2019, 2019.

Thomas, C. and Foken, T.: Organised motion in a tall spruce canopy: temporal scales, structure spacing and terrain effects, Boundary-Layer Meteorol., 122, 123–147, https://doi.org/10.1007/s10546-006-9087-z, 2007a.

Thomas, C. and Foken, T.: Flux contribution of coherent structures and its implications for the exchange of energy and matter in a tall spruce canopy, Boundary-Layer Meteorol., 123, 317–337, https://doi.org/10.1007/s10546-006-9144-7, 2007b.

Thomas, C. K. and Babel, W.: The Intramix data set, https://doi.org/10.5281/zenodo.4764490, 2021.

Thomas, C. K. and Levy, J. S.: The DRYVEXA data set, https://doi.org/10.5281/zenodo.4764499, https://doi.org/10.5281/zenodo.4764499, 2021.

Thomas, C. K., Vogl, T., and Hrdina, A.: The ExpMM data set, https://doi.org/10.5281/zenodo.4764493, 2021.

Vickers, D. and Mahrt, L.: Quality control and flux sampling problems for tower and aircraft data, J. Atmos. Ocean. Technol., 14, 512–526, 1997.

Vickers, D., Thomas, C., and Law, B. E.: Random and systematic CO2 flux sampling errors for tower measurements over forests in the convective boundary layer, Agric. For. Meteorol., 149, 73–83, https://doi.org/10.1016/j.agrformet.2008.07.005, 2009.

5 Webb, E., Pearman, G. I., and Leuning, R.: Correction of flux measurements for density effects due to heat and water vapor transfer, Quart. J. Roy. Meteor. Soc., 106, 85–100, 1980.

Wyngaard, J. C. and Moeng, C.-H.: Parameterizing turbulent diffusion through the joint probability density, Boundary Layer Meteorol., 60, 1–13, https://doi.org/10.1007/BF00122059, 1992.